Coral calcifying fluid aragonite saturation states derived from Raman spectroscopy

Thomas M. DeCarlo[1,2], Juan P. D'Olivo[1,2], Taryn Foster[3], Michael Holcomb[1,2], Thomas Becker[4,5], and Malcolm T. McCulloch[1,2]

[1]Oceans Institute and School of Earth Sciences, The University of Western Australia, 35 Stirling Hwy, Crawley 6009, Australia
[2]ARC Centre of Excellence for Coral Reef Studies, The University of Western Australia, 35 Stirling Hwy, Crawley 6009, Australia
[3]Australian Institute of Marine Science, Crawley 6009, Australia
[4]Centre for Microscopy, Characterisation and Analysis, The University of Western Australia, Crawley 6009, Australia
[5]Department of Chemistry, Curtin Institute of Functional Molecules and Interfaces, Curtin University, GPO Box U1987, Perth 6845, Australia

Correspondence to: Thomas M. DeCarlo (thomas.decarlo@uwa.edu.au)

Abstract. Quantifying the saturation state of aragonite (Ω_{Ar}) within the calcifying fluid of corals is critical for understanding their biomineralisation process and sensitivity to environmental changes including ocean acidification. Recent advances in microscopy, microprobes, and isotope geochemistry allow determination of calcifying fluid pH and $[CO_3^{2-}]$, but direct quantification of Ω_{Ar} (where $\Omega_{Ar}=[CO_3^{2-}][Ca^{2+}]/K_{sp}$) has proved elusive. Here we test a new technique for deriving Ω_{Ar} based on Raman spectroscopy. First, we analysed abiogenic aragonite crystals precipitated under a range of Ω_{Ar} from 10 to 34, and we found a strong dependence of Raman peak width on Ω_{Ar} with no significant effects of other factors including pH, Mg/Ca partitioning, and temperature. Validation of our Raman technique for corals is difficult because there are presently no direct measurements of calcifying fluid Ω_{Ar} available for comparison. However, Raman analysis of the international coral standard JCp-1 produced Ω_{Ar} of 12.3 ± 0.3, which we demonstrate is consistent with published skeletal Mg/Ca, Sr/Ca, B/Ca, $\delta^{11}B$, and $\delta^{44}Ca$ data. Raman measurements are rapid (≤ 1 s), high-resolution (≤ 1 μm), precise (derived $\Omega_{Ar} \pm 1$ to 2 per spectrum depending on instrument configuration), accurate (± 2 if $\Omega_{Ar} < 20$), and require minimal sample preparation; making the technique well suited for testing the sensitivity of coral calcifying fluid Ω_{Ar} to ocean acidification and warming using samples from natural and laboratory settings. To demonstrate this, we also show a high-resolution time series of Ω_{Ar} over multiple years of growth in a *Porites* skeleton from the Great Barrier Reef, and we evaluate the response of Ω_{Ar} in juvenile *Acropora* cultured under elevated CO_2 and temperature.

1 Introduction

The calcium carbonate ($CaCO_3$) skeletons built by coral polyps are the building blocks of massive coral reef structures that protect shorelines, bolster tourism, and host some of the greatest concentrations of biodiversity on the planet (Knowlton et al., 2010; Costanza et al., 2014). Critical to the coral calcification process is the extraction of Ca^{2+} and CO_3^{2-} ions from seawater

to grow aragonitic $CaCO_3$ crystals. But corals today live in seawater that is less conducive to $CaCO_3$ nucleation than it was just a century ago. In surface waters of the tropical oceans, carbonate ion concentrations ($[CO_3^{2-}]$) have declined by ~15% since 1900 due to invasion of anthropogenic CO_2, which dissociates into carbonic acid and decreases seawater pH and $[CO_3^{2-}]$ through a process referred to as ocean acidification (Caldeira and Wickett, 2003; Doney et al., 2009). If anthropogenic CO_2
5 emissions continue unabated, by the end of the 21st century the $[CO_3^{2-}]$ of surface seawater is projected to decline to ~50% of pre-industrial levels (Hoegh-Guldberg et al., 2014). This rapid change in ocean carbonate chemistry, likely unprecedented for hundreds of millions of years (Hönisch et al., 2012; Zeebe et al., 2016), has sparked concerns for coral growth. Indeed, laboratory experiments repeatedly demonstrate that coral calcification rates decrease in response to lower $[CO_3^{2-}]$ or $[Ca^{2+}]$ (Gattuso et al., 1998; Chan and Connolly, 2013; Comeau et al., 2017), leading to projections that as CO_2 levels continue to
10 rise calcification will decline to unsustainable levels, such that there is net reef erosion (Hoegh-Guldberg et al., 2007; Pandolfi et al., 2011).

Yet signs of resilience do exist. Some coral species are able to maintain normal calcification rates across large natural acidification gradients (Fabricius et al., 2011; Shamberger et al., 2014; Barkley et al., 2015), indicative of adaptation or acclimation (Barkley et al., 2017). One potential mechanism to counteract acidification of surrounding seawater is pH homeostasis at the
15 site of calcification (Georgiou et al., 2015; Barkley et al., 2017). Corals calcify from an isolated fluid located between the living tissue and the existing skeleton (Barnes, 1970; Cohen and McConnaughey, 2003; Venn et al., 2011; Tambutté et al., 2012). Up-regulation of pH within this fluid, potentially achieved via proton pumping and/or symbiont photosynthesis, elevates the saturation state with respect to aragonite (Ω_{Ar}), contributing to rapid nucleation and growth of aragonite crystals (Gattuso et al., 1999; Cohen and McConnaughey, 2003; Al-Horani et al., 2003; McCulloch et al., 2012; Kubota et al., 2015).
20 Characterising the Ω_{Ar} of the calcifying fluid, and understanding its sensitivities to variations in the reef environment, is therefore essential for accurately forecasting coral calcification responses to 21st century ocean acidification. Observing this fluid has proved difficult though, due to its small size and isolation beneath the living polyp (Clode and Marshall, 2002). Estimates of fluid carbonate chemistry have so far been derived from micro-electrodes, pH-sensitive dyes, boron isotopes, B/Ca, U/Ca, and bulk calcification rates (Al-Horani et al., 2003; Trotter et al., 2011; Venn et al., 2011; DeCarlo et al., 2015;
25 Cai et al., 2016; Holcomb et al., 2016; Raybaud et al., 2017). However, these approaches do not always agree (Ries, 2011; Holcomb et al., 2014), and they have so far focused on calcifying fluid carbonate chemistry without considering the effect of $[Ca^{2+}]$ on Ω_{Ar}.

A potential alternative approach to quantify calcifying fluid Ω_{Ar} is based on the Raman scattering from a laser focused onto the skeleton. When light interacts with a material, a small percent (typically <0.0001%) of the photons are scattered
30 inelastically (referred to as Raman or Stokes scattering), resulting in a change of energy and frequency (Smith and Dent, 2005). The frequency shifts associated with Raman scattering are characteristic of both the internal vibrations of a molecule and the lattice vibrations between molecules in a crystal, which makes Raman spectroscopy a valuable tool for mineral identification (Urmos et al., 1991; Dandeu et al., 2006; Brahmi et al., 2010; Clode et al., 2011; Nehrke et al., 2011; Stock et al., 2012; Foster and Clode, 2016; Stolarski et al., 2016; Roger et al., 2017). Importantly, Raman peaks can also provide information regarding the chemical composition of crystals and the conditions of the fluid from which they formed. For example, in abiogenic $CaCO_3$,

the shapes and positions of the ν_1 peak at ~1085 cm^{-1} (which represents symmetric stretching of the carbonate C-O bond) have been correlated with Mg content and/or crystallinity (Bischoff et al., 1985; Wang et al., 2012; Perrin et al., 2016). A highly crystalline CaCO$_3$ with relatively few defects or impurities will have a narrow ν_1 peak because the C-O bonds throughout the crystals are of the same, or very similar, length (Bischoff et al., 1985). Defects in the crystals and/or trace element impurities cause positional disorder of CO$_3$ in the lattice. Positional disorder affects the length, and thus the strength and vibrational frequency, of C-O bonds (Bischoff et al., 1985). An increase in disorder leads to an increase in the distribution of C-O bond lengths, causing an increase in ν_1 peak width (Bischoff et al., 1985; Addadi et al., 2003; Lin et al., 2007; Wang et al., 2012; McElderry et al., 2013; Perrin et al., 2016).

In biogenic calcium carbonates, correlations have been reported between ν_1 peak widths and environmental conditions, including temperature and seawater pCO$_2$ (Kamenos et al., 2013, 2016; Hennige et al., 2015; Pauly et al., 2015). These changes potentially reflect differences in calcifying fluid carbonate chemistry. Crystals growing from more supersaturated solutions generally have more defects and incorporate more impurities (Watson, 2004), resulting in relatively disordered crystal lattices and wide Raman peaks (Urmos et al., 1991). This hypothesis is generally consistent with empirical observations of biogenic calcium carbonates, in which ν_1 peak widths increase as ambient seawater pCO$_2$ decreases and/or pH increases (*i.e.* higher Ω_{Ar}) (Kamenos et al., 2013; Hennige et al., 2015; Pauly et al., 2015). However, corals exert strong control on the carbonate chemistry of their calcifying fluid by elevating pH and/or Ω_{Ar} at the site of calcification to facilitate more rapid crystal growth (Al-Horani et al., 2003; Venn et al., 2011; McCulloch et al., 2012). Thus, the observed correlations between Raman peak widths and ambient seawater conditions likely do not reflect the true sensitivity of aragonite Raman peaks to seawater chemistry, but rather the sensitivity of calcifying fluid chemistry to external pH and/or Ω_{Ar}. For this reason, information regarding the relationship between carbonate chemistry and Raman peak width in abiogenic experiments is required to quantitatively interpret Raman spectra of biogenic CaCO$_3$ with respect to the actual calcifying fluid conditions.

Here, we first evaluate the controls on Raman ν_1 peak width using abiogenically precipitated aragonites. These samples allow us to test the sensitivities of ν_1 peak width against geochemical composition (*e.g.* Mg/Ca) and fluid conditions (including Ω_{Ar}, pH and temperature) directly, without the confounding influence of a coral polyp. We derive a calibration between ν_1 peak width and Ω_{Ar}, and apply it to estimate Ω_{Ar} of the international coral skeleton standard JCp-1, for which independent lines of geochemical evidence allow us to test the accuracy of our approach. Finally, we demonstrate the applicability of Raman spectroscopy by (1) reconstructing multiple years of Ω_{Ar} variability in a *Porites* coral collected from the Great Barrier Reef (GBR) (D'Olivo and McCulloch, 2017), and (2) comparing Ω_{Ar} in cultured juvenile *Acropora spicifera* exposed to elevated CO$_2$ and temperature treatments (Foster et al., 2015).

2 Methods

2.1 Raman Measurements

Raman spectroscopy was used to analyse the abiogenic aragonite precipitates described in DeCarlo et al. (2015) and Holcomb et al. (2016) (Supplement Table S1). Briefly, aragonite was precipitated by addition of Na$_2$CO$_3$ and NaHCO$_3$ solutions to

seawater. Various $Na_2CO_3/NaHCO_3$ ratios and pumping rates produced a range of Ω_{Ar} from 10-34 while achieving some independence between Ω_{Ar} and other carbonate system variables (*e.g.* r^2 between Ω_{Ar} and pH was only 0.34). Most (22 of 28) experiments were conducted at 25.5 °C, but two experiments were conducted each at 20 °C, 33 °C, and 40 °C. Two

5   experiments (f08 and g13) were conducted from seawater with [Ca^{2+}] elevated by addition of dissolved $CaCO_3$.

Raman spectra of the abiogenic aragonites were originally reported in DeCarlo et al. (2015) and Holcomb et al. (2016). These initial spectra were collected at Woods Hole Oceanographic Institution (WHOI) with a Horiba LabRam HR800 Raman spectrometer using a 785 nm laser source, 40x objective, 600 mm^{-1} grating, and CCD detector maintained at -70 °C. Spectral resolution was approximately 1.2 cm^{-1}. Three grains were analysed per experiment with an integration time of 5 s per spec-

10   trum. Subsequently, we repeated analyses of a subset of these aragonites (samples f02, f03, f06, g07, g13, h09) at the Centre for Microscopy, Characterisation, and Analysis (CMCA) at the University of Western Australia. These more refined measurements, which are the basis of this study, were performed with a WITec Alpha300 RA+ confocal Raman microscope using a 785 nm laser source, 20x objective with numerical aperture of 0.5, 1200 mm^{-1} grating, and an Andor iDUS 401 CCD detector maintained at -60 °C. The nominal spectral resolution was 1.3 cm^{-1}. A silicon chip was analysed to facilitate comparison of

15   peak position with other laboratories (the strong Si peak was present at 522.9 cm^{-1}). For analysis of the abiogenic aragonites, at least five grains were analysed per experiment with 5-10 spectra per grain and integration times between 0.1 and 5 s (see Supplement for a comparison between instruments and discussion of the general applicability of our results to measurements in other laboratories). All analyses of coral skeletons described below were conducted with the WITec instrument using 1 s integration times.

20   The *Porites* coral skeleton standard JCp-1 (Okai et al., 2002) was analysed to facilitate comparison between Raman results and geochemical estimates of calcifying fluid Ω_{Ar} and [Ca^{2+}]. We collected 440 spectra from various grains spread onto a glass slide. Although JCp-1 exists in ground form, we note that analysis of intact coral skeletons is also possible (Wall and Nehrke, 2012; Hennige et al., 2014) and that peak widths apparently do not depend on whether the sample is powdered or intact (Zakaria et al., 2008), as long as the grain size exceeds the laser spot size.

25   We also collected Raman spectra down-core in a *Porites* skeleton collected from the Great Barrier Reef (the sample is described in detail in D'Olivo and McCulloch (2017). Briefly, the core was collected near Havannah Island, an in-shore reef in the central GBR where corals bleached during 1998. The skeleton was cut in a slab and cleaned with bleach as described by D'Olivo and McCulloch (2017), but no additional preparation was required. D'Olivo and McCulloch (2017) present $\delta^{11}B$ and trace element/Ca ratios from multiple tracks in the skeleton, and they show anomalies to the skeletal geochemistry corre-

30   sponding to the 1998 thermal stress event. We used the automated microscope stage and area-mapping features of the WITec instrument to measure Raman spectra in a down-core transect at 50-μm resolution, covering approximately 6 years of growth from 1996 to 2002. The TrueSurface module was used to construct a topography map of the skeleton that was then followed by the instrument to ensure the sample was always in-focus for the Raman measurements. A maximum depth of 1 mm below the cut surface was set to limit the integration of signal from skeleton of different ages. Each time-point represents the average of 10 spectra spaced horizontally in 100 μm increments.

5   Finally, we analysed skeletons of the cultured juvenile *Acropora* described in Foster et al. (2015, 2016). Briefly, larval planulae were maintained in "Control" (24 °C, 250 μatm CO_2), "+*T*" (27 °C, 250 μatm CO_2), "+CO_2" (24 °C, 900 μatm CO_2), and "+CO_2+*T*" (27 °C, 900 μatm CO_2) treatments. Raman data were previously reported for these corals in Foster and Clode (2016) but those earlier measurements were conducted with a 600 mm^{-1} grating, which made it difficult to resolve changes in peak width (see Supplement). We therefore collected 25 new Raman spectra from each of three broken skeletal pieces from each of three corals, per treatment. The TrueSurface module was used to ensure all measurements were taken with the optics well focused on the samples.

2.2   Calculations and Statistics

For all Raman spectra, we utilised the Full Width at Half Maximum intensity (FWHM) of the ν_1 peak (Fig. 1). A Gaussian-shaped curve was fitted to each spectrum between 1080 and 1100 cm^{-1} with the following expression:

$$y = b + mx + ke^{\frac{-(p-x)^2}{2s^2}} \tag{1}$$

where y is the fit, x is the Raman shift between 1080 and 1100 cm^{-1}, b is the background intensity, m is the background slope, k is the peak height, p is the peak position (*i.e.* wavenumber), and s is the standard deviation. Peak intensity varies depending on the smoothness of the surface and the focus of the laser. We removed spectra with ν_1 peak height < 30 intensity units (signal:noise of approximately 5) due to the larger uncertainties associated with curves fit to these spectra. FWHM is calculated following Weisstein (2017):

$$\text{FWHM} = 2s\sqrt{2\ln(2)} \approx 2.3548s \tag{2}$$

where s is the standard deviation of the Gaussian curve from equation (1). Measured Raman peak widths are known to be convolutions of the "true" peak widths and instrument noise (Nasdala et al., 2001; Wang et al., 2012; Váczi, 2014). The effect of instrument noise on Raman peak widths is directly related to the spectral resolution, which must be accounted for when comparing measurements conducted on different instruments (see Supplement). We used the Nasdala et al. (2001) formula to account for the effect of spectral resolution and calculate true FWHM:

$$b_t = b_m\sqrt{1 - 2(\frac{r_s}{b_m})^2} \tag{3}$$

where b_t is the true peak width, b_m is the measured peak width, and r_s is the spectral resolution.

In the analysis of the abiogenic aragonite, we used the linear model function in R (R Core Team, 2016) to test for relationships between ν_1 FWHM and Ω_{Ar}, aragonite precipitation rate, aragonite Mg/Ca, fluid [CO_3^{2-}], fluid pH, Raman peak height (k), and Raman peak position (p). Since Ω_{Ar} was the single variable most strongly correlated with ν_1 FWHM, we also evaluated linear models with two explanatory variables: Ω_{Ar} and the rest of the variables listed above. Analysis of variance (ANOVA)
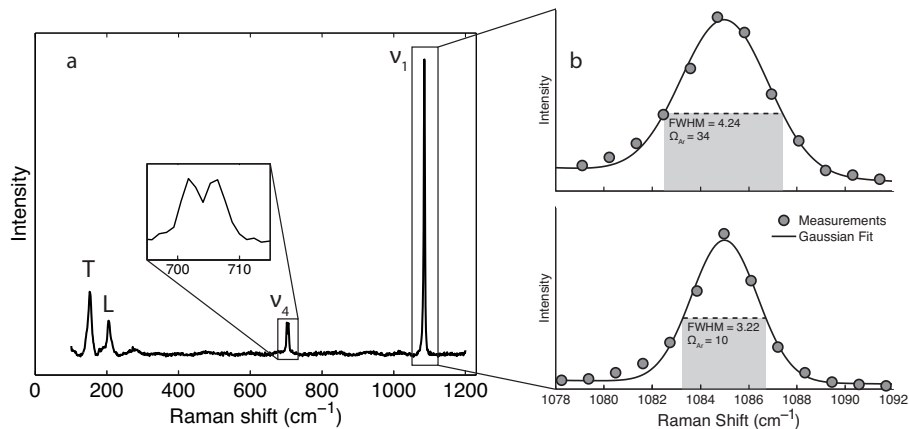
Figure 1. Example Raman spectra and peak width analyses. (a) Raman spectrum of precipitate from experiment f03, with the peaks labelled following White (1974) and Bischoff et al. (1985): T = translation (lattice mode), L = libration (lattice mode), ν_4 = in-plane bend (internal mode), and ν_1 = symmetric stretch (internal mode). This spectrum is readily identifiable as $CaCO_3$ based on the strong ν_1 peak at approximately 1085 cm^{-1}, and distinguished as aragonite rather than other $CaCO_3$ polymorphs (calcite and vaterite) based on the positions of the T, L, and ν_4 peaks (Dandeu et al., 2006). The double peak between 700-710 cm^{-1} is the feature that most clearly distinguishes aragonite from calcite or vaterite (Urmos et al., 1991). (b) Measurement of ν_1 peak width. The grey points are the measured intensities at the corresponding Raman wavenumber shift. The black lines show the Gaussian curves fit to the data, and the grey boxes indicate the measured peak widths (ν_1 FWHM). Note that measured ν_1 FWHM is converted to true ν_1 FWHM for analysis in subsequent figures. The y-axis scale is in arbitrary intensity units.

was used to test whether multivariate models were significantly better than the model based on Ω_{Ar} alone. We tested for normality of residuals with Kolmogorov-Smirnov tests and homogeneity of variances with Levene's test.

For the cultured *Acropora*, we calculated the mean Ω_{Ar} of each skeletal fragment using the abiogenic ν_1 FWHM-Ω_{Ar} calibration, weighting the 25 measurements per fragment by peak height. We then tested whether the data were significantly different from normal distributions with Kolmogorov-Smirnov tests and homogeneity of variances was checked with Levene's test. Finding no significant differences from normal distributions and no significant differences in variance among treatments, we conducted a two-way ANOVA and evaluated the effects with Tukey's honest significant difference test. Statistical significance was defined as $p < 0.05$.

2.3 Mg/Ca partitioning between aragonite and seawater

We also report here the partitioning of Mg/Ca between these abiogenic aragonites and seawater because (1) previous studies have suggested that Mg/Ca is important for interpreting Raman peak widths (Bischoff et al., 1985; Urmos et al., 1991), and (2) Mg/Ca is used as a constraint in our comparison of JCp-1 geochemistry and Raman spectroscopy. Partitioning of Mg^{2+}

between aragonite and seawater can be described by an exchange for Ca^{2+} in the aragonite lattice, with a partition coefficient (K_D) expressed as:

$$K_D^{\text{Mg/Ca}} = \frac{\frac{\text{Mg}}{\text{Ca}}_{aragonite}}{\frac{\text{Mg}}{\text{Ca}}_{seawater}} \tag{4}$$

where K_D is dimensionless (Kinsman and Holland, 1969; Gaetani and Cohen, 2006). While there is some uncertainty in the mechanism of Mg^{2+} incorporation into aragonite (Montagna et al., 2014), the K_D nevertheless serves as an empirical measure of the distribution of Mg/Ca between aragonite and seawater under various conditions. DeCarlo et al. (2015) reported K_D for Sr/Ca from these same samples, and here we follow the same calculations for $K_D^{\text{Mg/Ca}}$ using the Mg/Ca data from Holcomb et al. (2016), except for the slight modifications to the calculations described below. Briefly, $K_D^{\text{Mg/Ca}}$ was calculated from the measured Mg/Ca in the bulk precipitate (Holcomb et al., 2016), estimates of Mg/Ca in the initial fluid (seawater), and modelling the evolution of elemental concentrations in the fluid through the course of each experiment. However, since [Mg] in the initial seawater was not reported, we instead calculated initial [Mg] and [Ca] from the established relationships between salinity and concentrations of these elements in seawater (Riley and Tongudai, 1967). Our approach also differs from DeCarlo et al. (2015) in that they combined element/Ca measurements of both the final solution and the bulk solid to calculate K_D, whereas we used only the reported aragonite Mg/Ca because final fluid [Mg] was not measured. Two of the experiments (f08 and g13) were conducted with initial elemental concentrations modified from seawater by addition of dissolved $CaCO_3$, and they were excluded from $K_D^{\text{Mg/Ca}}$ calculations due to uncertainty of the fluid Mg/Ca ratio.

3   Results

In the abiogenic aragonites analysed in this study, ν_1 FWHM was strongly correlated with seawater Ω_{Ar} (r^2=0.70, p<0.001; Fig. 2 and Tables 1-2). Aragonite precipitation rate (G) is a function of Ω_{Ar} and temperature (T) (Burton and Walter, 1987), and thus the experiments conducted at different T allow us to isolate the influence of Ω_{Ar} from G. In contrast to the strong dependence of ν_1 FWHM on Ω_{Ar}, there was no significant correlation between ν_1 FWHM and G (Fig. 3; Table 1). ν_1 FWHM was significantly correlated with the aragonite Mg/Ca ratio, fluid [CO_3^{2-}], pH, T, and ν_1 peak height (Fig. 3; Table 1). However, these correlations were all weaker than the correlation between ν_1 FWHM and Ω_{Ar}, and in multivariate models combining Ω_{Ar} with either Mg/Ca, [CO_3^{2-}], pH, T, or ν_1 peak height, the only significant variable was Ω_{Ar} (Table 1). Together, this indicates that Ω_{Ar} is likely the variable controlling ν_1 FWHM, and that the correlations between ν_1 FWHM and other factors may arise as artefacts of the correlations between those variables and Ω_{Ar}. The relationship between Ω_{Ar} and ν_1 FWHM is shown in Table 2 for measured and true FWHM on both the Horiba and WITec instruments (see Supplement for alternate calibration where Ω_{Ar} is fit to ν_1 FWHM). Uncertainty of the calibration propagates to an accuracy of derived Ω_{Ar} of ±~2 for Ω_{Ar} < 20, but increases to ±~6 at Ω_{Ar}=30 due to both the logarithmic shape of the relationship and the distance from the regression center. The distributions of residuals were not significantly different from normal distributions (Kolmogorov-Smirnov test, p > 0.8). FWHM data for each experiment are listed in Supplement Table S2.
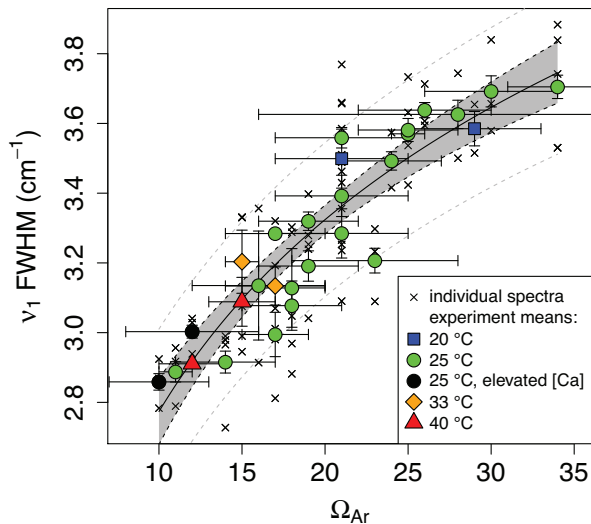
Figure 2. Sensitivity of true ν_1 FWHM to Ω_{Ar}. The x-axis represents the mean, and the horizontal error bars represent 1 standard deviation, of Ω_{Ar} while aragonite precipitated in each experiment. The crosses indicate individual spectra, the filled points indicate means of each experiment, and the vertical error bars represent the standard error of replicate spectra. Colours indicate experiments conducted at various temperatures, and black circles indicate the two experiments conducted with elevated [Ca^{2+}]. Grey shading represents the standard error of the curve fit to the individual spectra, and the dashed grey lines represent the standard error of prediction.

Some uncertainty exists in defining the Ω_{Ar} associated with each Raman spectrum, due to the variability of Ω_{Ar} over the course of each abiogenic experiment. We conducted a Monte Carlo simulation using the data from the Horiba instrument to evaluate the variability in ν_1 FWHM that is expected to arise from the uncertainty in Ω_{Ar}. In each of 10^4 Monte Carlo iterations, we added random error to the mean Ω_{Ar} of each experiment, based on the standard deviation of measured Ω_{Ar} and assuming a Gaussian distribution. Next, we calculated ν_1 FWHM in each iteration based on Ω_{Ar} (including the random error added) using the equation in Table 2. The average standard deviation of the Monte Carlo ν_1 FWHM residuals (the difference between the predicted and calculated ν_1 FWHM in each iteration) was 0.24 cm^{-1}, which is 50% greater than the observed standard deviation of the residuals (0.16 cm^{-1}). Since the simulated variability exceeds the observed variability, one or more of the following is implied: 1) most (or all) of the scatter in ν_1 FWHM around the regression line is explained by uncertainty of Ω_{Ar}, 2) the Raman spectra integrate signal from multiple crystals that together approximate the mean Ω_{Ar} during each experiment, and/or 3) variability in Ω_{Ar} is overestimated. Regardless, the data are consistent with a tight, logarithmic dependence of ν_1 FWHM on Ω_{Ar}, with scatter in Ω_{Ar} adding uncertainty to the observed relationship.

Analysis of 440 spectra collected from various grains of JCp-1 with the WITec instrument produced a mean measured ν_1 FWHM of 3.51 with 1σ of $\pm$ 0.09 cm^{-1} (true ν_1 FWHM of 2.99 $\pm$ 0.11 cm^{-1}). Applying the calibration equation in Table 2

Table 1. Linear model statistics for fits to ν_1 FWHM

Model:	F-value[a]	p-value(s)	r^2	Residual σ[b]
$\ln(\Omega_{Ar})$	186.4	**<0.001**	0.70	0.165
Mg/Ca	85.79	**<0.001**	0.52	0.210
G	0.77	0.383	0.0	0.304
CO_3^{2-}	133.9	**<0.001**	0.63	0.185
pH	35.46	**<0.001**	0.31	0.253
T	6.75	**0.011**	0.07	0.293
ν_1 height	4.50	**0.037**	0.04	0.297
ν_1 position	0.06	0.807	0.02	0.289
$\ln(\Omega_{Ar})$ + Mg/Ca	92.97	**<0.001**, 0.460	0.70	0.166
$\ln(\Omega_{Ar})$ + G	92.02	**<0.001**, 0.944	0.70	0.166
$\ln(\Omega_{Ar})$ + CO_3^{2-}	95.91	**<0.001**, 0.135	0.71	0.164
$\ln(\Omega_{Ar})$ + pH	97.43	**<0.001**, 0.079	0.71	0.163
$\ln(\Omega_{Ar})$ + T	92.18	**<0.001**, 0.755	0.70	0.166
$\ln(\Omega_{Ar})$ + ν_1 height	92.02	**<0.001**, 0.954	0.70	0.166

Notes: None of the multivariate models were significantly different from the Ω_{Ar} model. [a] 1,77 degrees of freedom for univariate models, and 2,76 degrees of freedom for multivariate models; except for ν_1 position, which had 1,59 degrees of freedom. [b] standard deviation (1 σ) of the ν_1 FWHM residuals from the model fit.

Table 2. Regression equations between mean ν_1 FWHM and Ω_{Ar}

Calibration:	Intercept	Slope	r^2	Residual σ
Horiba measured	1.62 (0.17)	0.70 (0.06)	0.85	0.09
Horiba true	0.94 (0.19)	0.79 (0.06)	0.85	0.11
WITec measured	2.09 (0.14)	0.57 (0.05)	0.96	0.05
WITec true	1.35 (0.16)	0.66 (0.06)	0.96	0.06

Notes: Equations describe ν_1 FWHM = slope$\times\ln(\Omega_{Ar})$ + intercept, where the regressions were performed on the mean values of each experiment. Parentheses indicate 1 standard error.
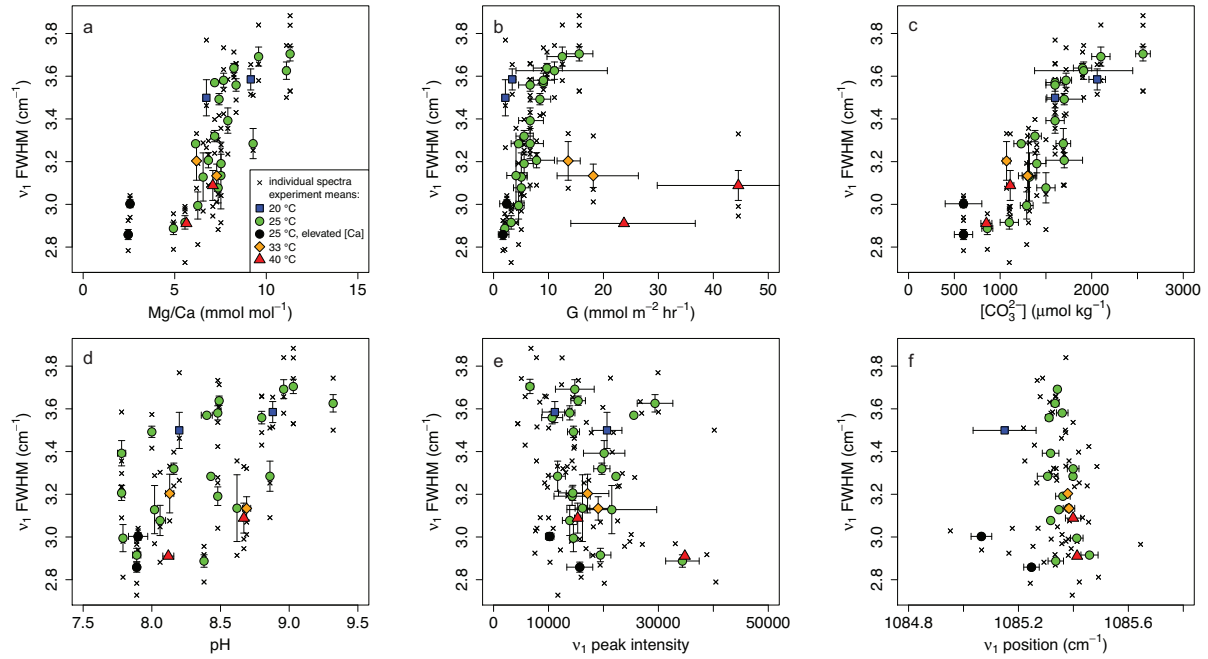
Figure 3. Scatter plots of Raman true peak width (ν_1 FWHM) and (a) aragonite Mg/Ca, (b) aragonite precipitation rate, (c) experimental fluid $[CO_3^{2-}]$, (d) experimental fluid pH, (e) Raman peak intensity, and (f) Raman peak position. Colours indicate experiments conducted at various temperatures, and black circles indicate the two experiments conducted with elevated $[Ca^{2+}]$. While some apparent correlations exist, statistical models (Table 1) imply that Ω_{Ar} is the variable controlling ν_1 FWHM, and that the patterns observed here may be artefacts of correlations between these factors and Ω_{Ar}.

to calculate Ω_{Ar} for each of the 440 measurements of ν_1 FWHM gave a mean derived Ω_{Ar} of 12.3, with a standard deviation
5   of 2.1, and a standard error of the mean of 0.3.

In the Havannah Island coral, measured ν_1 FWHM changed seasonally by ~0.15 cm^{-1}. Using our abiogenic calibration (Table 2) to estimate calcifying fluid Ω_{Ar}, these seasonal changes in FWHM translate to approximately 3 Ω_{Ar} units before the 1998 thermal stress event to approximately 1-2 Ω_{Ar} units afterwards.

Measured ν_1 FWHM of the cultured *Acropora* ranged from mean of 3.45 ($\pm$ 0.017 standard error) cm^{-1} for the control
10   treatment to 3.366 ($\pm$ 0.009 standard error) cm^{-1} for the "+CO$_2$+T" treatment. Derived Ω_{Ar} (from the abiogenic calibration) was significantly different among treatments. Tukey's test revealed significant decreases in Ω_{Ar} as both T (p < 0.001) and CO$_2$ (p = 0.045) increased. There was no significant interactive effect of T and CO$_2$.
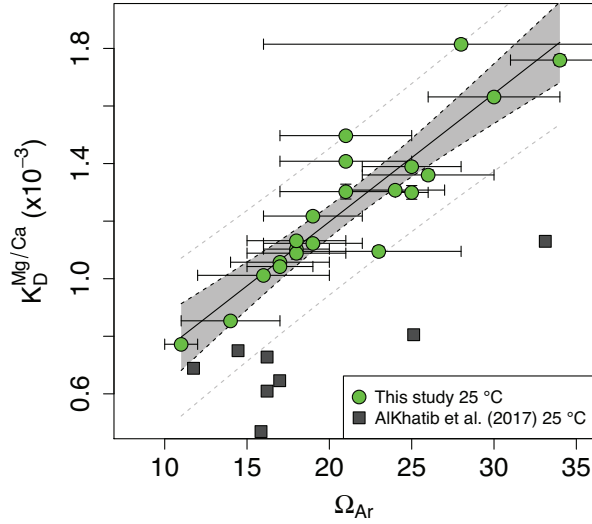
Figure 4. Sensitivity of $K_D^{\text{Mg/Ca}}$ to Ω_{Ar} at 25 °C. Horizontal error bars represent 1 standard deviation of Ω_{Ar} while aragonite precipitated in each experiment. Grey shading represents the standard error of the curve, and the dashed grey lines represent the standard error of prediction. The grey squares show the AlKhatib and Eisenhauer (2017) data replotted against Ω_{Ar} (*cf* their Fig. 4 for a plot against precipitation rate).

$K_D^{\text{Mg/Ca}}$ determined from the abiogenic aragonites was significantly positively correlated with Ω_{Ar} (Fig. 4; Supplement Table S1; $r^2 = 0.82$ for experiments conducted at 25 °C):

$$5 \quad K_D^{\text{Mg/Ca}} = \frac{(0.045 \pm 0.004)\Omega_{Ar} + 0.31 \pm 0.11}{1000} \tag{5}$$

The key finding of the $K_D^{\text{Mg/Ca}}$ data for this study is the sensitivity to Ω_{Ar} at a single temperature. This dependence of $K_D^{\text{Mg/Ca}}$ on Ω_{Ar} or precipitation rate was predicted by Gaetani and Cohen (2006) on the basis of the surface entrapment model proposed by Watson (2004), and was also observed in a recent abiogenic aragonite study (AlKhatib and Eisenhauer, 2017) (Fig. 4). Although our $K_D^{\text{Mg/Ca}}$ data show a similar trend to those of AlKhatib and Eisenhauer (2017), their $K_D^{\text{Mg/Ca}}$ are systematically
10   lower. This offset is potentially explained by the different media used in the experiments: filtered seawater in DeCarlo et al. (2015) and Holcomb et al. (2016) as opposed to ammonium carbonate solutions in AlKhatib and Eisenhauer (2017).

4 Discussion

4.1 Controls on aragonite ν_1 peak width

We conducted Raman spectroscopy analyses of abiogenic aragonites, precipitated under various carbonate chemistry and temperature treatments as previously described in DeCarlo et al. (2015) and Holcomb et al. (2016). Carbonate chemistry was manipulated in these experiments such that there is some independence between the carbonate system parameters, which allows us to isolate their effects on the Raman spectral peaks. For example, experiments conducted at the same Ω_{Ar}, but different temperatures, allow us to identify that ν_1 FWHM is sensitive to Ω_{Ar} but not to aragonite precipitation rate (G) (Figs. 2 and 3b). Similarly, since Sr/Ca is strongly controlled by temperature in these aragonites (DeCarlo et al., 2015), the lack of a temperature effect on ν_1 FWHM implies that Sr/Ca ratios exert minor or no effects on ν_1 FWHM. Other factors were more difficult to isolate, for instance Ω_{Ar} was correlated with both Mg/Ca$_{solid}$ and fluid [CO$_3^{2-}$]. Yet, comparisons among statistical models (Table 1) show that Ω_{Ar} is the only variable that consistently has a significant effect on ν_1 FWHM, regardless of which additional variable is considered in multivariate models. This leads us to conclude that ν_1 FWHM is primarily dependent upon Ω_{Ar}. We also found that the scattering of data around the regression between ν_1 FWHM and Ω_{Ar} can be explained entirely by the uncertainty of Ω_{Ar} in each experiment. Further, the absence of any significant correlations between ν_1 FWHM and either ν_1 position or height indicates that the variation of ν_1 FWHM in our study was not the result of instrumental or curve-fitting artefacts.

Our ability to isolate the effect of Ω_{Ar} from Mg/Ca$_{solid}$ and fluid [CO$_3^{2-}$] is best exemplified by the two experiments in which [Ca^{2+}] was elevated in the fluids by addition of dissolved CaCO$_3$. Experiments f08 and g13 were conducted with mean fluid Ω_{Ar} of 12 and 10, and [Ca^{2+}] of 12.4 and 10.4 mmol kg^{-1}, respectively, compared to the mean [Ca^{2+}] range of 6.9 - 8.7 mmol kg^{-1} in all other experiments. The addition of Ca^{2+} increased Ω_{Ar}, decreased Mg/Ca, and caused precipitation to occur at lower [CO$_3^{2-}$] than other experiments, thereby establishing some independence among these factors. Over the relatively narrow Ω_{Ar} range of 10 - 12, which includes f08 and g13 as well as two experiments with lower [Ca^{2+}], there is still a positive correlation between ν_1 FWHM and Ω_{Ar} (Fig. 5a). Conversely, there are no clear patterns between ν_1 FWHM and either Mg/Ca or [CO$_3^{2-}$] across these four experiments (Fig. 5b-c). While this further demonstrates that Ω_{Ar} is likely the factor directly controlling ν_1 FWHM, more experiments designed to decouple Ω_{Ar}, Mg/Ca and [CO$_3^{2-}$] will be useful for constraining ν_1 FWHM sensitivities. In addition, whether the stoichiometry of [Ca^{2+}] and [CO$_3^{2-}$] affects ν_1 FWHM will be an important question to address with future experiments (Nehrke et al., 2007)

The influence of Ω_{Ar} on ν_1 FWHM can be explained by carbonate ion disorder within the aragonite lattice, as originally hypothesized by Bischoff et al. (1985). Increasing Ω_{Ar} causes more defects and/or impurities to be incorporated into the aragonite, increasing the positional disorder of carbonate in the lattice. The absence of a clear Mg/Ca effect on ν_1 FWHM (discussed further below) suggests that our observed changes in ν_1 FWHM are related more to disorder in the lattice (*i.e.* more amorphous-like aragonites formed at higher Ω_{Ar}) than to trace element impurities. Disordered carbonate ions have a distribution of C-O bond strengths and vibrational frequencies, which results in wider Raman peaks (Bischoff et al., 1985; Urmos et al., 1991; Perrin et al., 2016).
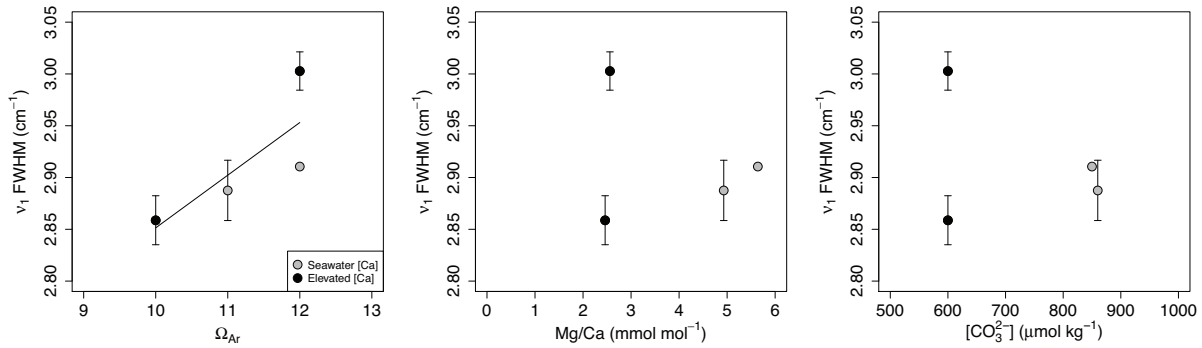
Figure 5. Isolation of Ω_{Ar}, Mg/Ca and [CO_3^{2-}] controls on true ν_1 FWHM based on manipulation of fluid [Ca^{2+}]. The same data are plotted here as in Figs. 2-3, but only over the Ω_{Ar} range of 10-12 because it includes two experiments initiated with seawater [Ca^{2+}] (grey) and two experiments with elevated [Ca^{2+}] (black). With fluid [Ca^{2+}] manipulation, ν_1 FWHM is still sensitive to Ω_{Ar} (panel a), but not to Mg/Ca (panel b) or [CO_3^{2-}] (panel c).

10   Raman spectroscopy studies of abiogenic $CaCO_3$ have so far focused on calcite, vaterite, and amorphous $CaCO_3$ (ACC) precipitated with wide ranges of Mg/Ca (from 0-45 mol%) (Bischoff et al., 1985; Wehrmeister et al., 2009; Wang et al., 2012; Perrin et al., 2016). These studies manipulated the Mg/Ca ratios of the solutions from which the precipitates formed, and they consistently reported strong correlations between ν_1 FWHM and ν_1 position, both of which increased with progressively higher Mg/Ca in the solid phase. The abiogenic precipitates used in our study are different in that (1) they are aragonite, and (2) most

15 of them (26 out of 28) were grown from the same parent solution (seawater) but under different carbonate chemistry treatments (DeCarlo et al., 2015; Holcomb et al., 2016). Most of the Mg/Ca variability in these aragonites arises from the sensitivity of Mg/Ca partitioning to Ω_{Ar} (Fig. 4), not manipulation of Mg/Ca in the initial fluid. Recognising this methodological distinction is important for understanding why we did not find a correlation between ν_1 FWHM and position. Firstly, aragonite has several orders of magnitude less Mg than high-Mg calcites, potentially dampening the role of Mg in affecting the shape of the Raman

20 peaks in aragonite. Secondly, if the trend between Ω_{Ar} and ν_1 FWHM were driven by Mg content alone, shifts in Raman peaks to higher wavenumbers would be expected because Mg is lighter than Ca (Bischoff et al., 1985). However, there was no significant correlation between ν_1 position and Ω_{Ar} (p > 0.7), indicating that the mean C-O bond vibrational frequency did not change systematically with Ω_{Ar}. These observations imply that Mg content was not the primary source of lattice defects broadening Raman peaks, an interpretation supported by the absence of a correlation between Mg/Ca and ν_1 FWHM (after

25 accounting for the effect of Ω_{Ar}; Table 1). The lack of correlation between ν_1 FWHM and position also indicates that ν_1 FWHM was unaffected by crystallite size (Urmos et al., 1991; Zakaria et al., 2008).

    That fluid Ω_{Ar}, not Mg/Ca$_{solid}$, apparently controls ν_1 FWHM in aragonite precipitated from seawater is critical for interpreting Raman spectra of coral skeletons. Corals transport seawater to the micro-scale site of calcification (Gagnon et al., 2012; Tambutté et al., 2012), and much like in the abiogenic experiments of DeCarlo et al. (2015) and Holcomb et al. (2016),

30   they precipitate aragonite crystals from a seawater-like solution (McConnaughey, 1989). Changes in calcifying fluid Mg/Ca can result from Ca^{2+} transport and/or Rayleigh fractionation (Gaetani and Cohen, 2006; Gagnon et al., 2012). Yet Mg/Ca in coral skeletons is generally within the limits of the abiogenic aragonites analysed here (2.5 - 11 mmol mol^{-1}), and critically, ν_1 FWHM was insensitive to Mg/Ca over this range. While it is still conceivable that Mg/Ca or [CO_3^{2-}] could have some influence on coral ν_1 FWHM, these effects are likely subordinate to the Ω_{Ar} sensitivity based on our abiogenic results. This implies that we can interpret Raman spectra of coral skeletons using the abiogenic sensitivity of ν_1 FWHM to Ω_{Ar}.

4.2   Analysis of JCp-1 and relation to skeletal geochemistry

  Using Raman spectroscopy, we derived a mean calcifying fluid Ω_{Ar} for the JCp-1 coral standard of 12.3 ± 0.3. JCp-1 is an

5   internationally calibrated geochemical standard, and has been analysed repeatedly for trace element and isotopic composition. Because the geochemistry of the skeleton reflects the calcifying fluid conditions, we can evaluate the accuracy of our Ω_{Ar} estimates by comparing them to the reported geochemical properties of the JCp-1 carbonate. Specifically, here we calculate calcifying fluid calcium concentration ([Ca^{2+}]$_{cf}$) using two different sets of proxies; the first based on Mg/Ca, Sr/Ca, and δ^{44}Ca, and the second based on Raman, δ^{11}B (a pH proxy), and B/Ca (see Appendix A for details of calculations). Our

10   approach uses experimentally determined partitioning of these trace elements and isotopes between aragonite and seawater, and a simple model in which [Ca^{2+}]$_{cf}$ is initially elevated relative to seawater (Al-Horani et al., 2003) before precipitation from the isolated calcifying fluid (*i.e.* a closed system) drives Rayleigh fractionation (Gaetani and Cohen, 2006; Gaetani et al., 2011; Gagnon et al., 2012). We then compare these two independent [Ca^{2+}]$_{cf}$ estimates to test whether our Raman results are consistent with JCp-1 geochemistry.

5   The published Mg/Ca, Sr/Ca and δ^{44}Ca of the JCp-1 coral can be explained with initial Ca^{2+} enrichment of 9-11% and precipitation of 48-59% of the total Ca^{2+}. This corresponds to mean [Ca^{2+}]$_{cf}$ of 8.2 ± 0.7 mmol kg^{-1} (Fig. 6). We then independently estimated [Ca^{2+}]$_{cf}$ by combining our Raman spectroscopy results with boron systematics. The δ^{11}B and B/Ca of JCp-1 together imply a calcifying fluid [CO_3^{2-}] of 987 ± 78 μmol kg^{-1}. To reconcile the boron-derived [CO_3^{2-}] with the Raman-derived Ω_{Ar} of 12.3 ± 0.3 requires [Ca^{2+}]$_{cf}$ of 8.3 ± 0.7 mmol kg^{-1}. This agrees almost exactly with the mean

10   [Ca^{2+}]$_{cf}$ based on the calculations described above for Mg/Ca, Sr/Ca, and δ^{44}Ca systematics (Fig. 6d), giving us confidence in the accuracy of our Raman-based Ω_{Ar} results. One implication of these results is that [Ca^{2+}]$_{cf}$ is less than seawater by 11-25%, and while this finding should be replicated on additional corals, we note that depleted [Ca^{2+}]$_{cf}$ is consistent with trace element variability in deep-sea and surface-dwelling corals modelled using both "batch" and "flow-through" versions of the Rayleigh calculations (Gaetani et al., 2011; Gagnon et al., 2012). Further, our Raman-derived Ω_{Ar} is generally consistent

15   with estimates made on the basis of coral skeleton crystal aspect ratios (Cohen and Holcomb, 2009).

4.3   High-resolution time series of calcifying fluid Ω_{Ar}

Analysis of the Havannah Island coral demonstrates that Raman spectroscopy can detect variability in coral calcifying fluid Ω_{Ar}. The pattern of variability in Raman-derived Ω_{Ar} showed some similarities, but also some differences, compared to the boron-derived Ω_{Ar} presented in D'Olivo and McCulloch (2017). In a sampling track that avoided a 1998 partial-mortality scar
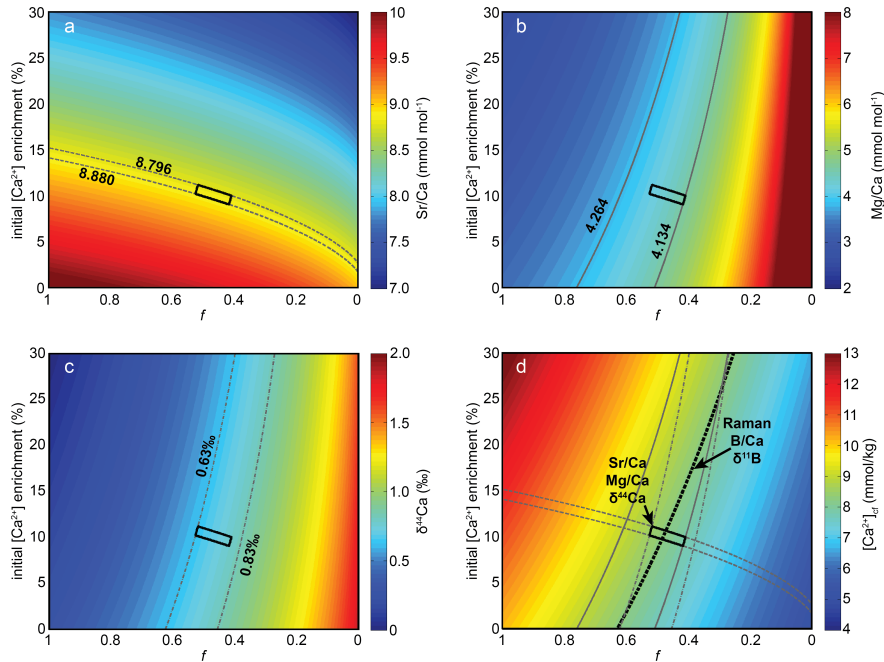
Figure 6. Evaluation of Raman-derived Ω_{Ar} based on geochemistry of the JCp-1 coral. In each panel, the x-axis f is fraction of total $[Ca^{2+}]_{cf}$ remaining, and the y-axis is initial $[Ca^{2+}]_{cf}$ enrichment relative to seawater. Colours indicate calculated (a) skeletal Sr/Ca, (b) skeletal Mg/Ca, (c) skeletal $\delta^{44}Ca$, and (d) $[Ca^{2+}]_{cf}$. In (a-c) the grey lines bound the reported values of JCp-1 ($\pm 1\sigma$), and the black polygon shows the parameter space consistent with Sr/Ca, Mg/Ca, and $\delta^{44}Ca$. Panel (d) shows $[Ca^{2+}]_{cf}$ and the grey lines show the constraints from panels (a-c). The dashed black line indicates the $[Ca^{2+}]_{cf}$ independently estimated based on combining our Raman data with published boron data (see text for details of the calculations). The two approaches are within error (*i.e.* the dashed black line intersects the solid black polygon) for Raman-derived Ω_{Ar} between 10.8 and 13.7, consistent with the observed Ω_{Ar} of 12.3 $\pm$ 0.3.

20   ("Path D"), boron-derived Ω_{Ar} showed annual oscillations of 2-3 units, but one seasonal oscillation was completely missing during 1998/1999 (Fig. 7). Yet in a track directly adjacent to the scar ("Path B"), boron-derived Ω_{Ar} showed overall lower values and less variability, compared to that from Path D. Raman-derived Ω_{Ar} closely tracked variability of Path D from 1996 to early 1998, then diverged from the boron-derived Ω_{Ar} between mid-1998 and mid-1999, before returning to similar seasonal variability by 2000.

25   There are several possible reasons for the differences between Raman- and boron- derived Ω_{Ar}. The first is that the Raman sampling path was located approximately halfway between boron Paths B and D, and thus there could be differences in Ω_{Ar} across the skeleton. The boron data indicate lower Ω_{Ar} near the partial-mortality scar while the Raman data potentially reflect an intermediate level of bleaching stress between the low values of Path B and the higher values of Path D. There is also potential for the existence of secondary precipitates near the scar, although the Raman spectra clearly indicated only

30 aragonite was present with no sign of calcite. Second, the Raman measurements have higher spatial resolution than the boron
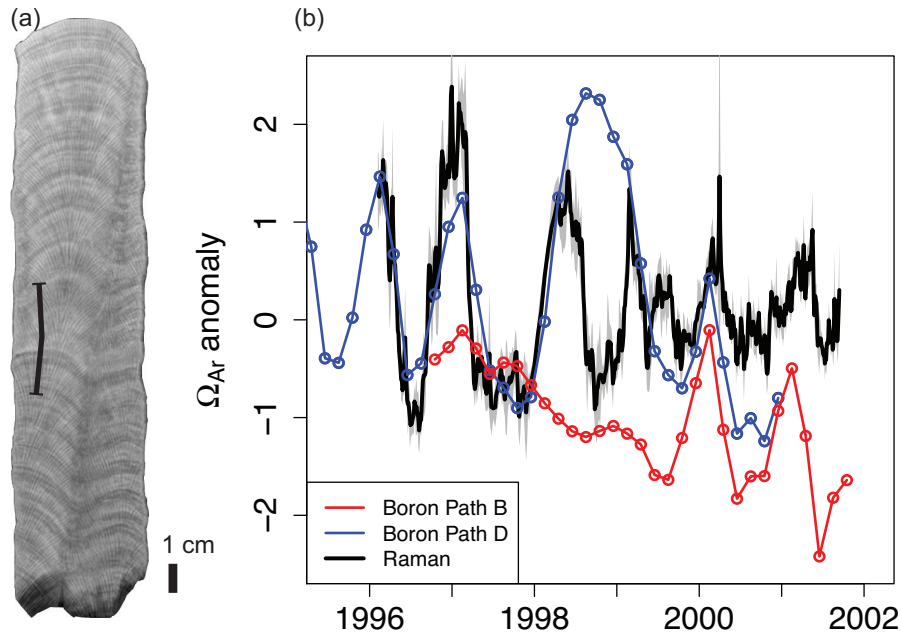
Figure 7. Time series of boron- and Raman-derived Ω_{Ar} in a coral from Havannah Island. (a) X-Ray image of central slab cut from the core. The black line indicates the Raman sampling path. Boron paths B and D were located approximately 1 cm into and out of the page, respectively (*cf.* Fig. 1 in D'Olivo and McCulloch (2017) for details). (b) The red and blue lines show boron-derived Ω_{Ar} assuming a constant $[Ca^{2+}]_{cf}$. Raman-derived Ω_{Ar} is plotted in black with grey error bars indicating 1 σ. The means of the two datasets (mean of Raman Ω_{Ar} was 9.5) have been removed to facilitate comparison and because of uncertainty of absolute $[Ca^{2+}]_{cf}$ for the boron calculations.

measurements, potentially allowing us to capture variability not observed in the boron sampling paths. Finally, boron-derived estimates of Ω_{Ar} are based on the assumption that $[Ca^{2+}]_{cf}$ remains at, or close to, seawater concentrations, and therefore any substantial changes in $[Ca^{2+}]_{cf}$ will not be recorded in the boron-derived time series. This means that the decoupling between Raman- and boron-derived Ω_{Ar} from Path D during 1998-1999 could reflect changes in $[Ca^{2+}]_{cf}$ (Fig. 7). D'Olivo and McCulloch (2017) showed that trace element ratios (Mg/Ca and Sr/Ca) in Path B indicated a strong reduction in $[Ca^{2+}]_{cf}$ during 1998, although a consistent pattern was not observed in Path D. Similarly, a recent study showed that Mg/Ca and Sr/Ca responses to bleaching in *Porites* from Western Australia were indicative of reduced $[Ca^{2+}]_{cf}$ (Clarke et al., 2017), consistent

5 with our comparison between Raman and boron systematics in the Havannah Island coral. Mechanistically, reduced $[Ca^{2+}]_{cf}$ could result from decreases in the renewal rates of calcifying fluid (via increased Rayleigh fractionation) or decreases in Ca^{2+} addition to the calcifying fluid. While more studies are needed to test if reduced $[Ca^{2+}]_{cf}$ is a consistent response to thermal stress, the ability to detect such changes by using Raman and boron systematics in tandem highlights their combined utility.
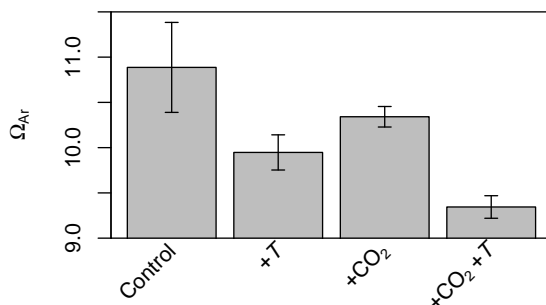
Figure 8. Raman-derived Ω_{Ar} of *Acropora* cultured under different temperature and CO_2 treatments. The grey bars indicate treatment means and error bars represent $\pm$ standard error of the mean. Significant effects were observed for both temperature and CO_2.

4.4   Effects of temperature and CO_2 on Ω_{Ar} of juvenile *Acropora*

Our analyses of juvenile *Acropora* indicate that calcifying fluid Ω_{Ar} decreased in response to elevated temperature (3 °C above the maximum monthly mean water temperature) and to elevated CO_2 (Fig. 8). In micro-computed tomography (micro-CT) analyses of corals from the same experiment, Foster et al. (2016) showed that elevated CO_2 increased skeletal porosity and decreased total calcification, while elevated temperature had the effect of partially mitigating the response to elevated CO_2. Thus, the effect of elevated CO_2 on Raman-derived Ω_{Ar} is consistent with the calcification response, but thermal stress decreased Ω_{Ar} without having a negative impact on calcification. One possibility is that the effect of decreasing Ω_{Ar} on aragonite accretion was balanced by elevated temperature because aragonite crystal growth rates increase with both Ω_{Ar} and temperature (Burton and Walter, 1987). Further, the physiological response to elevated temperature could be complex, potentially involving decreases in Ω_{Ar} balanced by increases in calcifying time or surface area. Finally, Foster et al. (2016) found pitted skeletal surfaces indicative of dissolution, which may have compounded the measured CO_2 effects on calcification and led to their dominance over any apparent effect of temperature in the "+CO_2+*T*" treatment. A recent study employing a similar experimental design found that juvenile *Acropora* B/Ca and U/Ca increased with elevated CO_2 (Wu et al., 2017), both of which indicate decreases in calcifying fluid [CO_3^{2-}] based on abiogenic partitioning (DeCarlo et al., 2015; Holcomb et al., 2016). However, while elevated temperature increased $\delta^{11}B$ (*i.e.* increased pH) it did not affect B/Ca or U/Ca (Wu et al., 2017), potentially reflecting the lower degree of thermal stress (culture temperatures were within the seasonal range at the collection site) compared to Foster et al. (2015) and/or that [Ca^{2+}]$_{cf}$ played an important role in our Raman data. Nevertheless, our results further highlight that Raman spectroscopy can detect changes in coral calcifying fluid Ω_{Ar}, and that this information is complementary to other analyses, including boron systematics (section 4.3) as well as CT-derived porosity and calcification.

5 Conclusions and Outlook

We tested whether Raman spectroscopy records the saturation state of the fluid from which aragonite precipitates. In abiogenic aragonites with known fluid conditions, we found a clear dependence of Raman peak width on Ω_{Ar}, an observation that is not confounded by other factors, including temperature, Mg/Ca, pH, and $[CO_3^{2-}]$. In the JCp-1 coral standard, for which calcifying fluid Ω_{Ar} is not known directly, Raman-derived Ω_{Ar} is consistent with multiple, independent lines of geochemical evidence based on Mg/Ca, Sr/Ca, B/Ca, $\delta^{11}B$, and $\delta^{44}Ca$. These results support the use of Raman spectroscopy as a proxy for coral calcifying fluid Ω_{Ar}. While it remains theoretically possible for other factors such as trace element variability to have some influence, our Raman results from abiogenic aragonites and the JCp-1 coral can be explained by Ω_{Ar} alone. Nevertheless, future investigations of controls on Raman spectra of corals skeleton will be useful, for instance by checking for positive correlations between ν_1 FWHM and wavenumber that would potentially indicate an effect of Mg/Ca (Bischoff et al., 1985; Perrin et al., 2016; Borromeo et al., 2017). We found no such relationships in either our *Porites* or *Acropora* analyses (p > 0.05, $r^2 < 0.01$ in both cases).

Our approach could potentially be applied to other marine calcifiers that build aragonitic shells and skeletons, such as sclerosponges and some molluscs. However, the relationship between Raman peak width and Ω is likely to be mineral-specific. For example, calcite often contains magnesium with concentrations several orders of magnitude greater than in aragonite, which is likely the reason for the wider peaks in Raman spectra of calcite (Urmos et al., 1991). In contrast, we have shown that Raman spectroscopy is well suited for analysis of coral calcifying fluid Ω_{Ar}. Our initial applications to corals revealed annual cycles of Raman-derived Ω_{Ar} in a field-collected *Porites* and Ω_{Ar} responses to elevated temperature and CO_2 in cultured *Acropora*, highlighting that Raman spectroscopy is indeed capable of detecting changes in coral calcifying fluid Ω_{Ar}. Additionally, the high spatial resolution (< 1 μm) and rapid sample processing (≤ 1 s per spectrum) of Raman are currently unrivalled. Further, the same Raman spectra used to estimate Ω_{Ar} can confirm that the sample is aragonite, effectively eliminating the possibility of contamination from other mineral phases. Finally, our analysis of JCp-1 suggests that the Raman ν_1 FWHM may be an accurate proxy of fluid Ω_{Ar}, making it a complementary approach to B/Ca and $\delta^{11}B$ because combining information from the two approaches enables calculating the full carbonate system via $[CO_3^{2-}]$, pH and possibly now $[Ca^{2+}]_{cf}$.

The Ω_{Ar} of 12.3 that we derived for JCp-1 corresponds to an instantaneous inorganic (Burton and Walter, 1987) aragonite precipitation rate of 0.2 g cm^{-2} yr^{-1}. This result is somewhat surprising because the average annual calcification rate of *Porites* living at 25 °C is typically 1.3 g cm^{-2} yr^{-1} (Lough, 2008), a factor of x6.5 faster than expected on the basis of the inorganic calcifying fluid Ω_{Ar} systematics. Since coral calyces have complex 3-dimensional shape such that their skeletal surface area is actually much greater than the planar area of the colony surface (Barnes, 1970), this implies that calcifying surface area is an important factor in determining coral calcification rates (D'Olivo and McCulloch, 2017) and it complicates the use of bulk calcification rates for estimating Ω_{Ar} (Raybaud et al., 2017). Multiple studies using micro-CT have shown increases in porosity and surface area:volume ratios in corals cultured under elevated CO_2 levels (Tambutté et al., 2015; Foster et al., 2016). This may represent a strategy for controlling calcifying surface area (*i.e.* the area over which crystals are precipitating from the calcifying fluid at a given time) to maintain bulk calcification rates and partially offset the impacts of ocean acidification.

In summary, recent studies and technological advances in boron isotope measurements (McCulloch et al., 2014), CT (De-Carlo and Cohen, 2016; Foster et al., 2016) and Raman spectroscopy (this study) are now making it increasingly feasible to quantify coral calcification responses with a multi-pronged approach. Future investigations combining Raman spectroscopy with B/Ca, δ^{11}B, and porosity measurements on corals grown under elevated CO_2 will be valuable for understanding mechanisms of resilience to ocean acidification. These include pH homeostasis, maintenance of high calcifying fluid Ω_{Ar} by $[Ca^{2+}]$ or $[CO_3^{2-}]$ regulation, and increases in calcifying surface area as potential strategies for coral calcification to persist in a high-CO_2 world. Evaluating their relative importance in the face of both increasing reef-water temperature and declining $[CO_3^{2-}]$ will be critical to informing our predictions of where and when resilience may be found.

6   Code availability

An R code for Raman curve fitting is included in the Supplement. Codes for the full analysis is available at: https://codeocean.com/2017/06/30/code-for-quot-coral-calcifying-fluid-aragonite-saturation-states-derived-from-raman-spectroscopy-quot/.

7   Data availability

Raman data are summarised in the Supplement. Individual Raman spectra are available in the Code Ocean link above and in the Zenodo "Raman spectra of marine calcifiers" community (https://zenodo.org/communities/calcifierraman/) at http://doi.org/10.5281/zenodo.1035493.

Appendix A: Details of JCp-1 geochemistry calculations

The JCp-1 coral grew at an average temperature of 25 °C (Okai et al., 2002), and the mean salinity in the area is 34.54 (Levitus, 2010). At 25 °C, the $K_D^{\mathrm{Sr/Ca}}$ is 1.123 (DeCarlo et al., 2015), and at 25 °C and Ω_{Ar} of 12, $K_D^{\mathrm{Mg/Ca}}$ is ~6.5($\pm$0.5)x10^{-4} (Fig. 4; in agreement with the mean value of AlKhatib and Eisenhauer (2017) at < 20 Ω_{Ar} and within error of our regression). We calculated a range of possible skeletal Sr/Ca and Mg/Ca ratios based on various combinations of Ca^{2+} pumping (enrichment of initial $[Ca^{2+}]_{cf}$ relative to seawater between 0 and 30%) and Rayleigh fractionation (0-100% of total Ca^{2+} precipitated), and we compared the results to the known Sr/Ca (8.838 $\pm$ 0.042 mmol mol^{-1}) and Mg/Ca (4.199 $\pm$ 0.065 mmol mol^{-1}) ratios of JCp-1 (Fig. 6) (Hathorne et al., 2013). For δ^{44}Ca, we used the abiogenic aragonite fractionation factor (Gussone et al., 2003, 2005), seawater δ^{44}Ca = 1.88‰ (Hippler et al., 2003), Ca added via Ca-ATPase (*i.e.* $[Ca^{2+}]_{cf}$ enrichment) of 0.68‰ (Inoue et al., 2015), and an average coral skeleton δ^{44}Ca of 0.73 $\pm$ 0.1 (Inoue et al., 2015; Chen et al., 2016; Gothmann et al., 2016). Our calculation scheme utilised the Rayleigh equation:

$$\frac{i}{j}_{coral} = \frac{i}{j}_{initial\ fluid}\frac{(1-f^{D})}{1-f} \tag{A1}$$

where i/j is Mg/Ca, Sr/Ca, or ^{44}Ca/^{40}Ca, f is the fraction of Ca remaining, D is $K_D^{\mathrm{Mg/Ca}}$, $K_D^{\mathrm{Sr/Ca}}$, or α_{44-40}, and it is assumed that Mg and Sr concentrations in the initial fluid prior to precipitation are equal to those of seawater.

A similar result is achieved when considering the calcifying fluid as semi-closed and using the steady-state "flow-through" model of Gagnon et al. (2012). We used the same $K_D^{\mathrm{Mg/Ca}}$ and $K_D^{\mathrm{Sr/Ca}}$ listed above and the equations of Gagnon et al. (2012) to solve for their "γ" term (defined as the ratio of calcium pumping to precipitation) that best fit the JCp-1 data (0.35). Next, we found the unique value of "$\frac{P}{kz\rho}$" (3.1 mmol Ca kg^{-1}; where P is precipitation flux, k is seawater exchange rate, z is the ratio of calcifying volume to surface area, and ρ is

seawater density) that was consistent with this γ and the JCp-1 Mg/Ca and Sr/Ca. Finally, using these terms matched to JCp-1 geochemistry, we follow the equation given in Gagnon et al. (2012):

$$[\text{Ca}^{2+}]_{cf} = [\text{Ca}^{2+}]_{seawater} - \frac{(1-\gamma)P}{kz\rho} \tag{A2}$$

The $[\text{Ca}^{2+}]_{cf}$ calculated by this method is 8.1 mmol kg^{-1}, within error of the 8.2 $\pm$ 0.7 mmol kg^{-1} derived from our "batch" model calculations above (see Fig. 6).

Our second approach to calculating $[\text{Ca}^{2+}]_{cf}$ combines Raman spectroscopy with boron systematics. JCp-1 has a B/Ca ratio of 459.6 $\pm$ 22.7 μmol/mol (1σ) (Hathorne et al., 2013) and δ^{11}B of 24.3 $\pm$ 0.17‰ (1σ) (McCulloch et al., 2014). We used the isotope fractionation factor of Klochko et al. (2006) to determine pH from δ^{11}B assuming seawater δ^{11}B of 39.6‰ (Foster et al., 2010). Next, we used the parameterisation of pK$_B$ from Dickson (1990) to calculate [B(OH)$_4^-$] from pH, temperature, salinity, and assuming [B] equal to seawater (411 μmol kg^{-1} at salinity 34.54) (Allison et al., 2014). The $K_D^{\text{B/Ca}}$ of Holcomb et al. (2016) was used to determine [CO$_3^{2-}$] from measured B/Ca and calculated [B(OH)$_4^-$] (computer code available at https://codeocean.com/2017/05/08/boron-systematics-of-aragonite/interface, and see McCulloch et al. (2017)). We then solve for $[\text{Ca}^{2+}]_{cf}$ with the following formula:

$$[\text{Ca}^{2+}]_{cf} = \frac{\Omega_{Ar}}{[\text{CO}_3^{2-}]} K_{sp} \tag{A3}$$

where Ω_{Ar} is derived from Raman spectroscopy and K_{sp} is the solubility product of aragonite in seawater. $[\text{Ca}^{2+}]_{cf}$ calculated in this way is 8.3 $\pm$ 0.7 mmol kg^{-1}.

In the first set of calculations with Mg/Ca, Sr/Ca, and δ^{44}Ca, we assume only that Ca^{2+} is added to the fluid, whereas in the second set of calculations with Raman spectroscopy and boron systematics we assume carbonate chemistry is modified from seawater. However, since we do not directly connect the initial Ca^{2+} enrichment of the fluid with the carbonate system calculations, we do not need to make assumptions regarding the stoichiometry of any potential proton-Ca^{2+} exchange.

Author contributions. T.M.D. conceived the idea, designed the study, conducted Raman measurements, and analysed the data. M.H., J.P.D., T.F., and M.T.M. contributed materials and aided in the interpretation of results. T.M.D. wrote the manuscript and all authors contributed to revising the final version.

Competing interests. The authors declare no competing interests.

Acknowledgements. We thank all those who contributed to the materials used in this study. The abiogenic aragonites were precipitated in the laboratories of Dr. Glenn Gaetani and Dr. Anne Cohen at Woods Hole Oceanographic Institution (WHOI). For the study of the GBR coral, H. Clarke and K. Rankenburg at University of Western Australia provided laboratory and analytical assistance. Facilities and technical assistance for the *Acropora* culturing experiments were provided by the Batavia Coast Maritime Institute, with logistical and technical support from A. Basile and T. Basile. Frieder Klein (WHOI) assisted with the initial Raman measurements. Funding was provided by an ARC Laureate Fellowship (FL120100049) awarded to Professor Malcolm McCulloch and the ARC Centre of Excellence for Coral Reef Studies (CE140100020). The authors acknowledge the facilities, and the scientific and technical assistance of the Australian Microscopy & Microanalysis Research Facility at the Centre for Microscopy, Characterisation & Analysis, The University of Western Australia, a facility

funded by the University, the Western Australian State and Commonwealth Governments. Jan Fietzke and one anonymous reviewer provided constructive comments that improved a previous version of this manuscript.

30

References

Addadi, L., Raz, S., and Weiner, S.: Taking advantage of disorder: amorphous calcium carbonate and its roles in biomineralization, Advanced Materials, 15, 959–970, 2003.

Al-Horani, F. A., Al-Moghrabi, S. M., and De Beer, D.: The mechanism of calcification and its relation to photosynthesis and respiration in the scleractinian coral *Galaxea fascicularis*, Marine Biology, 142, 419–426, doi:10.1007/s00227-002-0981-8, 2003.

AlKhatib, M. and Eisenhauer, A.: Calcium and Strontium Isotope Fractionation during Precipitation from Aqueous Solutions as a Function of Temperature and Reaction Rate; II. Aragonite, Geochimica et Cosmochimica Acta, 209, 320–342, doi:10.1016/j.gca.2017.04.012, 2017.

Allison, N., Cohen, I., Finch, A. A., Erez, J., and Tudhope, A. W.: Corals concentrate dissolved inorganic carbon to facilitate calcification., Nature communications, 5, 5741, doi:10.1038/ncomms6741, 2014.

Barkley, H. C., Cohen, A. L., Golbuu, Y., Starczak, V. R., DeCarlo, T. M., and Shamberger, K. E.: Changes in coral reef communities across a natural gradient in seawater pH, Science Advances, 1, e1500 328, 2015.

Barkley, H. C., Cohen, A. L., McCorkle, D. C., and Golbuu, Y.: Mechanisms and thresholds for pH tolerance in Palau corals, Journal of Experimental Marine Biology and Ecology, 489, 7–14, doi:10.1016/j.jembe.2017.01.003, 2017.

Barnes, D. J.: Coral skeletons: an explanation of their growth and structure, Science, 170, 1305–1308, doi:10.1126/science.170.3964.1305, 1970.

Bischoff, W. D., Sharma, S. K., and MacKenzie, F. T.: Carbonate ion disorder in synthetic and biogenic magnesian calcites; a Raman spectral study, American Mineralogist, 70, 581–589, 1985.

Borromeo, L., Zimmermann, U., Andò, S., Coletti, G., Bersani, D., Basso, D., Gentile, P., Schulz, B., and Garzanti, E.: Raman spectroscopy as a tool for magnesium estimation in Mg-calcite, Journal of Raman Spectroscopy, 48, 983–992, doi:10.1002/jrs.5156, 2017.

Brahmi, C., Meibom, A., Smith, D. C., Stolarski, J., Auzoux-Bordenave, S., Nouet, J., Doumenc, D., Djediat, C., and Domart-Coulon, I.: Skeletal growth, ultrastructure and composition of the azooxanthellate scleractinian coral *Balanophyllia regia*, Coral Reefs, 29, 175–189, 2010.

Burton, E. A. and Walter, L. M.: Relative precipitation rates of aragonite and Mg calcite from seawater: Temperature or carbonate ion control?, Geology, 15, 111–114, 1987.

Cai, W.-J., Ma, Y., Hopkinson, B. M., Grottoli, A. G., Warner, M. E., Ding, Q., Hu, X., Yuan, X., Schoepf, V., Xu, H., Han, C., Melman, T. F., Hoadley, K. D., Pettay, D. T., Matsui, Y., Baumann, J. H., Levas, S., Ying, Y., and Wang, Y.: Microelectrode characterization of coral daytime interior pH and carbonate chemistry., Nature communications, 7, 11 144, doi:10.1038/ncomms11144, 2016.

Caldeira, K. and Wickett, M. E.: Anthropogenic carbon and ocean pH, Nature, 425, 365, 2003.

Chan, N. C. S. and Connolly, S. R.: Sensitivity of coral calcification to ocean acidification: a meta-analysis, Global Change Biology, 19, 282–290, doi:10.1111/gcb.12011, 2013.

Chen, X., Deng, W., Zhu, H., Zhang, Z., Wei, G., and McCulloch, M. T.: Assessment of coral $\delta^{44/40}$Ca as a paleoclimate proxy in the Great Barrier Reef of Australia, Chemical Geology, 435, 71–78, doi:10.1016/j.chemgeo.2016.04.024, 2016.

Clarke, H., D'Olivo, J. P., Falter, J., Zinke, J., Lowe, R., and McCulloch, M.: Differential response of corals to regional mass-warming events as evident from skeletal Sr/Ca and Mg/Ca ratios, Geochemistry, Geophysics, Geosystems, 18, 1794–1809, doi:10.1002/2016GC006788, 2017.

Clode, P. and Marshall, A.: Low temperature FESEM of the calcifying interface of a scleractinian coral, Tissue and Cell, 34, 187–198, doi:10.1016/S0040-8166(02)00031-9, 2002.

Clode, P. L., Lema, K., Saunders, M., and Weiner, S.: Skeletal mineralogy of newly settling *Acropora millepora* (Scleractinia) coral recruits, Coral Reefs, 30, 1–8, doi:10.1007/s00338-010-0673-7, 2011.

Cohen, A. L. and Holcomb, M.: Why corals care about ocean acidification: uncovering the mechanism, Oceanography, 22, 118–127, doi:10.5670/oceanog.2009.102, 2009.

35 Cohen, A. L. and McConnaughey, T. A.: Geochemical Perspectives on Coral Mineralization, Rev. Mineral. Geochem., 54, 151–187, doi:10.2113/0540151, 2003.

Comeau, S., Tambutté, E., Carpenter, R. C., Edmunds, P. J., Evensen, N. R., Allemand, D., Ferrier-Pagès, C., Tambutté, S., and Venn, A. A.: Coral calcifying fluid pH is modulated by seawater carbonate chemistry not solely seawater pH, Proceedings of the Royal Society of London B: Biological Sciences, 284, 2017.

Costanza, R., de Groot, R., Sutton, P., van der Ploeg, S., Anderson, S. J., Kubiszewski, I., Farber, S., and Turner, R. K.: Changes in the global value of ecosystem services, Global Environmental Change, 26, 152–158, doi:http://dx.doi.org/10.1016/j.gloenvcha.2014.04.002, 2014.

Dandeu, A., Humbert, B., Carteret, C., Muhr, H., Plasari, E., and Bossoutrot, J. M.: Raman Spectroscopy – A Powerful Tool for the Quanti-
5 tative Determination of the Composition of Polymorph Mixtures: Application to $CaCO_3$ Polymorph Mixtures, Chemical Engineering & Technology, 29, 221–225, doi:10.1002/ceat.200500354, 2006.

DeCarlo, T. M. and Cohen, A. L.: coralCT: software tool to analyze computerized tomography (CT) scans of coral skeletal cores for calcifi-cation and bioerosion rates, doi:10.5281/zenodo.57855, http://zenodo.org/record/57855, 2016.

DeCarlo, T. M., Gaetani, G. A., Holcomb, M., and Cohen, A. L.: Experimental determination of factors controlling U/Ca of arag-
10 onite precipitated from seawater: implications for interpreting coral skeleton, Geochimica et cosmochimica acta, 162, 151–165, doi:doi:10.1016/j.gca.2015.04.016, 2015.

Dickson, A. G.: Standard potential of the reaction: AgCl (s)+ 1/2H_2 (g)= Ag (s)+ HCl (aq), and the standard acidity constant of the ion HSO_4^- in synthetic sea water from 273.15 to 318.15 K, The Journal of Chemical Thermodynamics, 22, 113–127, 1990.

D'Olivo, J. P. and McCulloch, M. T.: Response of coral calcification and calcifying fluid composition to thermally induced bleaching stress,
15 Scientific Reports, 7, 2207, 2017.

Doney, S. C., Fabry, V. J., Feely, R. A., and Kleypas, J. A.: Ocean acidification: the other CO_2 problem, Marine Science, 1, doi:10.1146/annurev.marine.010908.163834, 2009.

Fabricius, K. E., Langdon, C., Uthicke, S., Humphrey, C., Noonan, S., De'ath, G., Okazaki, R., Muehllehner, N., Glas, M. S., and Lough, J. M.: Losers and winners in coral reefs acclimatized to elevated carbon dioxide concentrations, Nature Climate Change, 1, 165–169,
20 2011.

Foster, G. L., Pogge von Strandmann, P. A. E., and Rae, J. W. B.: Boron and magnesium isotopic composition of seawater, Geochemistry, Geophysics, Geosystems, 11, Q08 015, doi:10.1029/2010GC003201, 2010.

Foster, T. and Clode, P. L.: Skeletal mineralogy of coral recruits under high temperature and pCO_2, Biogeosciences, 13, 1717–1722, doi:10.5194/bg-13-1717-2016, 2016.

25 Foster, T., Gilmour, J. P., Chua, C. M., Falter, J. L., and McCulloch, M. T.: Effect of ocean warming and acidification on the early life stages of subtropical *Acropora spicifera*, Coral Reefs, 34, 1217–1226, doi:10.1007/s00338-015-1342-7, 2015.

Foster, T., Falter, J. L., McCulloch, M. T., and Clode, P. L.: Ocean acidification causes structural deformities in juvenile coral skeletons, Science Advances, 2, e1501 130–e1501 130, doi:10.1126/sciadv.1501130, 2016.

Gaetani, G. A. and Cohen, A. L.: Element partitioning during precipitation of aragonite from seawater: A framework for understanding
30 paleoproxies, Geochimica et cosmochimica acta, 70, 4617–4634, doi:10.1016/j.gca.2006.07.008, 2006.

Gaetani, G. A., Cohen, A. L., Wang, Z., and Crusius, J.: Rayleigh-Based, Multi-Element Coral Thermometry: a Biomineralization Approach to Developing Climate Proxies, Geochimica et cosmochimica acta, 75, 1920–1932, doi:10.1016/j.gca.2011.01.010, 2011.

Gagnon, A. C., Adkins, J. F., and Erez, J.: Seawater transport during coral biomineralization, Earth and Planetary Science Letters, 329, 150–161, 2012.

35 Gattuso, J.-P., Frankignoulle, M., Bourge, I., Romaine, S., and Buddemeier, R.: Effect of calcium carbonate saturation of seawater on coral calcification, Global and Planetary Change, 18, 37–46, doi:10.1016/S0921-8181(98)00035-6, 1998.

Gattuso, J. P., Allemand, D., and Frankignoulle, M.: Photosynthesis and calcification at cellular, organismal and community levels in coral reefs: a review on interactions and control by carbonate chemistry, American Zoologist, 39, 160–183, doi:http://dx.doi.org/10.1093/icb/39.1.160, 1999.

Georgiou, L., Falter, J., Trotter, J., Kline, D. I., Holcomb, M., Dove, S. G., Hoegh-Guldberg, O., and McCulloch, M.: pH homeostasis during coral calcification in a free ocean CO_2 enrichment (FOCE) experiment, Heron Island reef flat, Great Barrier Reef, Proceedings of the

5 National Academy of Sciences, 112, 13 219–13 224, doi:10.1073/pnas.1505586112, 2015.

Gothmann, A. M., Bender, M. L., Blättler, C. L., Swart, P. K., Giri, S. J., Adkins, J. F., Stolarski, J., and Higgins, J. A.: Calcium isotopes in scleractinian fossil corals since the Mesozoic: Implications for vital effects and biomineralization through time, Earth and Planetary Science Letters, 444, 205–214, doi:10.1016/j.epsl.2016.03.012, 2016.

Gussone, N., Eisenhauer, A., Heuser, A., Dietzel, M., Bock, B., Böhm, F., Spero, H. J., Lea, D. W., Bijma, J., and Nägler, T. F.: Model

10 for kinetic effects on calcium isotope fractionation (δ^{44}Ca) in inorganic aragonite and cultured planktonic foraminifera, Geochimica et Cosmochimica Acta, 67, 1375–1382, doi:10.1016/S0016-7037(02)01296-6, 2003.

Gussone, N., Böhm, F., Eisenhauer, A., Dietzel, M., Heuser, A., Teichert, B. M., Reitner, J., Wörheide, G., and Dullo, W.-C.: Calcium isotope fractionation in calcite and aragonite, Geochimica et Cosmochimica Acta, 69, 4485–4494, doi:10.1016/j.gca.2005.06.003, 2005.

Hathorne, E. C., Gagnon, A., Felis, T., Adkins, J., Asami, R., Boer, W., Caillon, N., Case, D., Cobb, K. M., Douville, E., DeMenocal, P.,

15 Eisenhauer, A., Garbe-Schönberg, D., Geibert, W., Goldstein, S., Hughen, K., Inoue, M., Kawahata, H., Kölling, M., Cornec, F. L., Linsley, B. K., McGregor, H. V., Montagna, P., Nurhati, I. S., Quinn, T. M., Raddatz, J., Rebaubier, H., Robinson, L., Sadekov, A., Sherrell, R., Sinclair, D., Tudhope, A. W., Wei, G., Wong, H., Wu, H. C., and You, C.-F.: Interlaboratory study for coral Sr/Ca and other element/Ca ratio measurements, Geochemistry, Geophysics, Geosystems, 14, 3730–3750, doi:10.1002/ggge.20230, 2013.

Hennige, S. J., Morrison, C. L., Form, A. U., Büscher, J., Kamenos, N. A., and Roberts, J. M.: Self-recognition in corals facilitates deep-sea

20 habitat engineering, Scientific Reports, 4, 6782, doi:10.1038/srep06782, 2014.

Hennige, S. J., Wicks, L. C., Kamenos, N. A., Perna, G., Findlay, H. S., and Roberts, J. M.: Hidden impacts of ocean acidification to live and dead coral framework., Proceedings. Biological sciences / The Royal Society, 282, 20150 990, doi:10.1098/rspb.2015.0990, 2015.

Hippler, D., Schmitt, A.-D., Gussone, N., Heuser, A., Stille, P., Eisenhauer, A., and Nägler, T. F.: Calcium Isotopic Composition of Various Reference Materials and Seawater, Geostandards and Geoanalytical Research, 27, 13–19, doi:10.1111/j.1751-908X.2003.tb00709.x, 2003.

25 Hoegh-Guldberg, O., Mumby, P. J., Hooten, A. J., Steneck, R. S., Greenfield, P., Gomez, E., Harvell, C. D., Sale, P. F., Edwards, A. J., and Caldeira, K.: Coral reefs under rapid climate change and ocean acidification, Science, 318, 1737–1742, doi:10.1126/science.1152509, 2007.

Hoegh-Guldberg, O., Cai, R., Poloczanska, E., Brewer, P., Sundby, S., Helmi, K., Fabry, V., and Jung, S.: The Ocean, in: Climate Change 2014: Impacts, Adaptation, and Vulnerability. Contribution of Working Group 2 to the Fifth Assessment Report of the Intergovernmental

30 Panel on Climate Change, edited by Barros, V., Field, C., Dokken, D., Mastrandrea, M., Mach, K., Bilir, T., Chatterjee, M., Ebi, K.,

Estrada, Y., Genova, R., Girma, B., Kissel, E., Levy, A., MacCracken, S., Mastrandrea, P., and White, L., Cambridge University Press, Cambridge, United Kingdom and New York, NY, USA, 2014.

Holcomb, M., Venn, A. A., Tambutté, E., Tambutté, S., Allemand, D., Trotter, J., and McCulloch, M.: Coral calcifying fluid pH dictates response to ocean acidification, Scientific Reports, 4, 2014.

35 Holcomb, M., DeCarlo, T., Gaetani, G., and McCulloch, M.: Factors affecting B/Ca ratios in synthetic aragonite, Chemical Geology, 437, 67–76, doi:10.1016/j.chemgeo.2016.05.007, 2016.

Hönisch, B., Ridgwell, A., Schmidt, D. N., Thomas, E., Gibbs, S. J., Sluijs, A., Zeebe, R., Kump, L., Martindale, R. C., and Greene, S. E.: The geological record of ocean acidification, Science, 335, 1058–1063, doi:10.1126/science.1208277, 2012.

Inoue, M., Gussone, N., Koga, Y., Iwase, A., Suzuki, A., Sakai, K., and Kawahata, H.: Controlling factors of Ca isotope fractionation in scleractinian corals evaluated by temperature, pH and light controlled culture experiments, Geochimica et Cosmochimica Acta, 167,
5 80–92, doi:10.1016/j.gca.2015.06.009, 2015.

Kamenos, N. A., Burdett, H. L., Aloisio, E., Findlay, H. S., Martin, S., Longbone, C., Dunn, J., Widdicombe, S., and Calosi, P.: Coralline algal structure is more sensitive to rate, rather than the magnitude, of ocean acidification, Global Change Biology, 19, 3621–3628, 2013.

Kamenos, N. A., Perna, G., Gambi, M. C., Micheli, F., and Kroeker, K. J.: Coralline algae in a naturally acidified ecosystem persist by maintaining control of skeletal mineralogy and size, Proceedings of the Royal Society of London B: Biological Sciences, 283, 2016.

10 Kinsman, D. J. J. and Holland, H. D.: The co-precipitation of cations with $CaCO_3$-IV. The co-precipitation of Sr^{2+} with aragonite between 16 and 96 C, Geochimica et cosmochimica acta, 33, 1–17, doi:10.1016/0016-7037(69)90089-1, 1969.

Knowlton, N., Brainard, R. E., Fisher, R., Moews, M., Plaisance, L., and Caley, M.: Coral Reef Biodiversity, in: Life in the World's Oceans: Diversity, Distribution, and Abundance, 2010.

Kubota, K., Yokoyama, Y., Ishikawa, T., and Suzuki, A.: A new method for calibrating a boron isotope paleo-pH proxy using massive *Porites*
15 corals, Geochemistry, Geophysics, Geosystems, 16, 3333–3342, doi:10.1002/2015GC005975, 2015.

Levitus, S.: NOAA Atlas NESDIS 68-71, US Government Printing Office, Washington, D.C., 2010.

Lin, F., Sum, A. K., and Bodnar, R. J.: Correlation of methane Raman ν_1 band position with fluid density and interactions at the molecular level, Journal of Raman Spectroscopy, 38, 1510–1515, doi:10.1002/jrs.1804, 2007.

Lough, J.: Coral calcification from skeletal records revisited, Marine Ecology Progress Series, 373, 257–264, doi:10.3354/meps07398, 2008.

20 McConnaughey, T.: ^{13}C and ^{18}O isotopic disequilibrium in biological carbonates: I. Patterns, Geochimica et Cosmochimica Acta, 53, 151–162, doi:10.1016/0016-7037(89)90282-2, 1989.

McCulloch, M. T., Falter, J., Trotter, J., and Montagna, P.: Coral resilience to ocean acidification and global warming through pH up-regulation, Nature Climate Change, 2, 623–627, 2012.

McCulloch, M. T., Holcomb, M., Rankenburg, K., and Trotter, J. A.: Rapid, high-precision measurements of boron isotopic compositions in
25 marine carbonates, Rapid Communications in Mass Spectrometry, 28, 2704–2712, doi:10.1002/rcm.7065, 2014.

McCulloch, M. T., D'Olivo Cordero, J. P., Falter, J., Holcomb, M., and Trotter, J. A.: Coral calcification in a changing World: the interactive dynamics of pH and DIC up-regulation, Nature Communications, 8, 15 686, 2017.

McElderry, J.-D. P., Zhu, P., Mroue, K. H., Xu, J., Pavan, B., Fang, M., Zhao, G., McNerny, E., Kohn, D. H., Franceschi, R. T., Holl, M. M., Tecklenburg, M. M., Ramamoorthy, A., and Morris, M. D.: Crystallinity and compositional changes in carbonated apatites: Evidence from
30 ^{31}P solid-state NMR, Raman, and AFM analysis, Journal of Solid State Chemistry, 206, 192–198, doi:10.1016/j.jssc.2013.08.011, 2013.

Montagna, P., McCulloch, M., Douville, E., López Correa, M., Trotter, J., Rodolfo-Metalpa, R., Dissard, D., Ferrier-Pagès, C., Frank, N., Freiwald, A., Goldstein, S., Mazzoli, C., Reynaud, S., Rüggeberg, A., Russo, S., and Taviani, M.: Li/Mg systematics in scleractinian corals: Calibration of the thermometer, Geochimica et Cosmochimica Acta, 132, 288–310, doi:10.1016/j.gca.2014.02.005, 2014.

Nasdala, L., Wenzel, M., Vavra, G., Irmer, G., Wenzel, T., and Kober, B.: Metamictisation of natural zircon: accumulation versus thermal annealing of radioactivity-induced damage, Contributions to Mineralogy and Petrology, 141, 125–144, doi:10.1007/s004100000235, 2001.

Nehrke, G., Reichart, G., Van Cappellen, P., Meile, C., and Bijma, J.: Dependence of calcite growth rate and Sr partitioning on solution stoichiometry: Non-Kossel crystal growth, Geochimica et Cosmochimica Acta, 71, 2240–2249, doi:10.1016/J.GCA.2007.02.002, 2007.

Nehrke, G., Nouet, J., and Treude, T.: Confocal Raman microscope mapping as a tool to describe different mineral and organic phases at high spatial resolution within marine biogenic carbonates: case study on *Nerita undata* (Gastropoda, Neritopsina), Biogeosciences, 8, 3761–3769, 2011.

Okai, T., Suzuki, A., Kawahata, H., Terashima, S., and Imai, N.: Preparation of a New Geological Survey of Japan Geochemical Reference Material: Coral JCp-1, Geostandards Newsletter, 26, 95–99, doi:10.1111/j.1751-908X.2002.tb00627.x, 2002.

Pandolfi, J. M., Connolly, S. R., Marshall, D. J., and Cohen, A. L.: Projecting coral reef futures under global warming and ocean acidification, Science, 333, 418–422, 2011.

Pauly, M., Kamenos, N. A., Donohue, P., and LeDrew, E.: Coralline algal Mg-O bond strength as a marine pCO$_2$ proxy, Geology, 43, 267–270, doi:10.1130/G36386.1, 2015.

Perrin, J., Vielzeuf, D., Laporte, D., Ricolleau, A., Rossman, G. R., and Floquet, N.: Raman characterization of synthetic magnesian calcites, American Mineralogist, 101, 2525–2538, 2016.

R Core Team: R: A language and environment for statistical computing, 2016.

Raybaud, V., Tambutté, S., Ferrier-Pagès, C., Reynaud, S., Venn, A. A., Tambutté, É., Nival, P., and Allemand, D.: Computing the carbonate chemistry of the coral calcifying medium and its response to ocean acidification, Journal of Theoretical Biology, 424, 26–36, doi:10.1016/j.jtbi.2017.04.028, 2017.

Ries, J. B.: A physicochemical framework for interpreting the biological calcification response to CO$_2$-induced ocean acidification, Geochimica et cosmochimica acta, 75, 4053–4064, 2011.

Riley, J. P. and Tongudai, M.: The major cation/chlorinity ratios in sea water, Chemical Geology, 2, 263–269, 1967.

Roger, L. M., George, A. D., Shaw, J., Hart, R. D., Roberts, M., Becker, T., McDonald, B. J., and Evans, N. J.: Geochemical and microstructural characterisation of two species of cool-water bivalves (*Fulvia tenuicostata* and *Soletellina biradiata*) from Western Australia, Biogeosciences, 14, 1721–1737, doi:10.5194/bg-14-1721-2017, 2017.

Shamberger, K. E., Cohen, A. L., Golbuu, Y., McCorkle, D. C., Lentz, S. J., and Barkley, H. C.: Diverse coral communities in naturally acidified waters of a Western Pacific reef, Geophys. Res. Lett., 41, 499–504, doi:10.1002/2013GL058489 Key, 2014.

Smith, E. and Dent, G.: Modern Raman spectroscopy: a practical approach, John Wiley & Sons, West Sussex, England, 2005.

Stock, S. R., Veis, A., Xiao, X., Almer, J. D., and Dorvee, J. R.: Sea urchin tooth mineralization: Calcite present early in the aboral plumula, Journal of Structural Biology, 180, 280–289, doi:10.1016/j.jsb.2012.08.004, 2012.

Stolarski, J., Bosellini, F. R., Wallace, C. C., Gothmann, A. M., Mazur, M., Domart-Coulon, I., Gutner-Hoch, E., Neuser, R. D., Levy, O., Shemesh, A., and Meibom, A.: A unique coral biomineralization pattern has resisted 40 million years of major ocean chemistry change., Scientific reports, 6, 27 579, doi:10.1038/srep27579, 2016.

Tambutté, E., Tambutté, S., Segonds, N., Zoccola, D., Venn, A., Erez, J., and Allemand, D.: Calcein labelling and electrophysiology: insights on coral tissue permeability and calcification, Proceedings of the Royal Society B: Biological Sciences, 279, 19–27, doi:10.1098/rspb.2011.0733, 2012.

Tambutté, E., Venn, A. A., Holcomb, M., Segonds, N., Techer, N., Zoccola, D., Allemand, D., and Tambutté, S.: Morphological plasticity of the coral skeleton under CO_2-driven seawater acidification, Nature Communications, 6, 7368, doi:10.1038/ncomms8368, 2015.

640 Trotter, J., Montagna, P., McCulloch, M., Silenzi, S., Reynaud, S., Mortimer, G., Martin, S., Ferrier-Pagès, C., Gattuso, J. P., and Rodolfo-Metalpa, R.: Quantifying the pH 'vital effect' in the temperate zooxanthellate coral *Cladocora caespitosa*: Validation of the boron seawater pH proxy, Earth and Planetary Science Letters, 303, 163–173, 2011.

Urmos, J., Sharma, S. K., and Mackenzie, F. T.: Characterization of some biogenic carbonates with Raman spectroscopy, American Mineralogist, 76, 641–646, 1991.

645 Váczi, T.: A New, Simple Approximation for the Deconvolution of Instrumental Broadening in Spectroscopic Band Profiles, Applied Spectroscopy, 68, 1274–1278, doi:10.1366/13-07275, 2014.

Venn, A., Tambutte, E., Holcomb, M., Allemand, D., and Tambutte, S.: Live tissue imaging shows reef corals elevate pH under their calcifying tissue relative to seawater, PLoS One, 6, e20 013, doi:10.1371/journal.pone.0020013, 2011.

Wall, M. and Nehrke, G.: Reconstructing skeletal fiber arrangement and growth mode in the coral *Porites lutea* (Cnidaria, Scleractinia): a
650 confocal Raman microscopy study, Biogeosciences, 9, 4885–4895, 2012.

Wang, D., Hamm, L. M., Bodnar, R. J., and Dove, P. M.: Raman spectroscopic characterization of the magnesium content in amorphous calcium carbonates, Journal of Raman Spectroscopy, 43, 543–548, 2012.

Watson, E. B.: A conceptual model for near-surface kinetic controls on the trace-element and stable isotope composition of abiogenic calcite crystals, Geochimica et cosmochimica acta, 68, 1473–1488, 2004.

655 Wehrmeister, U., Soldati, A. L., Jacob, D. E., Häger, T., and Hofmeister, W.: Raman spectroscopy of synthetic, geological and biological vaterite: a Raman spectroscopic study, Journal of Raman Spectroscopy, 41, 193–201, doi:10.1002/jrs.2438, 2009.

Weisstein, E.: Gaussian Function, http://mathworld.wolfram.com/GaussianFunction.html, 2017.

White, W.: The carbonate minerals, in: The Infra-red Spectra of minerals, edited by Farmer, V., pp. 227–284, Mineralogical Society, London, 1974.

660 Wu, H. C., Dissard, D., Le Cornec, F., Thil, F., Tribollet, A., Moya, A., and Douville, E.: Primary Life Stage Boron Isotope and Trace Elements Incorporation in Aposymbiotic *Acropora millepora* Coral under Ocean Acidification and Warming, Frontiers in Marine Science, 4, 129, doi:10.3389/fmars.2017.00129, 2017.

Zakaria, F. Z., Mihály, J., Sajó, I., Katona, R., Hajba, L., Aziz, F. A., and Mink, J.: FT-Raman and FTIR spectroscopic characterization of biogenic carbonates from Philippine venus seashell and *Porites* sp. coral, Journal of Raman Spectroscopy, 39, 1204–1209,
665 doi:10.1002/jrs.1964, 2008.

Zeebe, R. E., Ridgwell, A., and Zachos, J. C.: Anthropogenic carbon release rate unprecedented during the past 66 million years, Nature Geoscience, 9, 325–329, doi:10.1038/ngeo2681, 2016.